Crack imaging by scanning laser-line thermography and laser-spot thermography

2011 Meas. Sci. Technol. 22 035701

(http://iopscience.iop.org/0957-0233/22/3/035701)

Meas. Sci. Technol. **22** (2011) 035701 (14pp) doi:10.1088/0957-0233/22/3/035701

Crack imaging by scanning laser-line thermography and laser-spot thermography

T Li, D P Almond and D A S Rees

UK Research Centre in NDE (RCNDE), Department of Mechanical Engineering, University of Bath, Claverton Down, Bath, BA2 7AY, UK

E-mail: D.P.Almond@bath.ac.uk

Received 1 June 2010, in final form 22 November 2010
Published 1 February 2011
Online at stacks.iop.org/MST/22/035701

Abstract
The thermographic images of laser-heated spots or lines are perturbed by nearby cracks, providing NDE techniques for crack detection. Scanning with a laser line, rather than a laser spot, results in a substantial reduction in inspection time. 3D finite difference modelling results are presented that show the sensitivity of the laser-line thermography technique to cracks of varying lengths, depths and openings. A novel crack imaging technique is presented that is based on assembling the second spatial derivative thermal images of a scanned laser line. Experimental results show the new technique to image cracks with openings as small as a few micrometres. The scanning time of the laser-line thermography technique is shown to be over an order of magnitude smaller than that of the laser-spot thermography technique whilst producing crack images of similar quality.

Keywords: nondestructive evaluation, cracks, laser, thermography

(Some figures in this article are in colour only in the electronic version)

1. Introduction

Pulsed, or transient, thermography [1–4] is the most widely used form of thermographic non-destructive evaluation (NDE). In this technique, a surface area is flash heated by one or more flash lamps and images of the subsequent cooling of the surface are collected by an infrared (IR) camera. The flash lamp heating produces an approximately uniform area of heating across a surface and this results in, essentially, one-dimensional heat flow from the surface into the bulk of the heated part. This limits the types of defects or features that can be detected by this technique to those that substantially alter the one-dimensional heat flow from the surface. Examples of such defects or features are delaminations lying in a plane parallel with the surface or interfaces between a surface coating and its substrate. Defects such as cracks, that form in planes that are essentially perpendicular to a surface, are not detectable by this technique. However, cracks of this type can be detected if the heating is localized to a spot or a line on a surface. Furthermore, thermal microscope measurements showed that thermally obtained lengths of a vertical crack in silicon nitride were at least 34% longer than those that were optically measured [5]. This paper presents an investigation of crack imaging using laser-spot and laser-line heating variants of pulsed thermography.

Previous workers have generated heating at a spot on a surface using electron or ion beams [6, 7], a focused arc lamp or a laser beam [8–16]. For line heating [17–25], methods have included a line infrared lamp, heated wire (radio frequency induction heating) [17, 18] or a line of air jets [19]. Where the heating is produced by the absorption of light, these methods are called photothermal techniques [22]. In much of the previous work using spot and line heating sources, an infrared detector was used for the detection of the heating. These applications are generally referred to as being 'photothermal radiometry' techniques rather than 'thermography'; the latter indicating the application of an IR camera.

In laser-spot or laser-line photothermal radiometry [8–11, 14–34], the surface heating at a point a distance away from the laser spot or laser line is monitored by a single IR

detector. At such a point, the heating provides a measure of the thermal impedance between the heated spot and the detection location. This impedance increases if a defect-restricting heat flow is present between the two points. Laser-spot or laser-line photothermal radiometry is typically performed by moving the laser spot or the laser line over the test piece at a fixed speed with a point-reading IR detector trained a fixed distance behind the spot or line. The methods presented here are laser-spot thermography and laser-line thermography (LST and LLT) in which an IR camera is used to collect full-frame images of all the heating produced by a laser spot or line. A complete inspection of a test piece is achieved by image processing thermal images collected during raster scanning the spot or line over the test piece surface.

Until recently, IR camera-based systems have required relatively expensive and bulky equipment, whilst an IR detector system could be an inexpensive and compact device [20, 24]. In addition, the response rates of IR detectors far exceeded the frame rates of the IR cameras. However, both the prices and the sizes of a modern IR camera are reducing and the response times of cameras are now in the range of 0.16–30 ms [35]. A major advantage of an IR camera is that it has a larger effective IR detection area than an IR detector. The spatial resolution of an IR detector-based system in the lateral direction (scanning direction) depends on the heated area and the resolution of the scanner [22, 26, 27]. For high resolution, a small detector area is required. However, a small detector collects less radiation which decreases the signal, leading to a deterioration in the system signal to noise ratio. By contrast, an IR camera has an array of detectors. The effective detection area is large and the resolution of the system can also be kept high due to the small size of the elements in the array.

In addition, if a single detector was used having a small detection area (perhaps in the range of 25–100 μm), scan steps of similar dimensions are needed to form a high resolution image of a surface. Thus the corresponding scan time will be long. An IR camera-based technique has the advantage of producing high resolution images using a far coarser (and faster) scanning raster because images are collected from the array of points around the heated spot or line that can be combined by image processing techniques, as will be shown below.

In this paper, an investigation of LLT as a means of detecting and imaging cracks is presented. Details of a similar investigation of LST have been published elsewhere [12, 13, 36]. Numerical modelling results are presented in section 2 that show similarities in the characteristics of the two techniques and the sensitivity of the LTT technique to crack geometry. A novel LLT crack imaging technique is presented in section 3. Experimental results obtained by both LLT and LST are compared in section 4.

2. 3D analytical and numerical modelling

2.1. 3D analytical modelling—point and line heating

There are no 3D analytical results for the distribution of a heat flow in a material containing narrow vertical cracks. However, results are available for the temperature rise caused by a laser source in a homogeneous, isotropic and semi-infinite material, such as metal. The 3D heat conduction in such a material can be expressed as [37, 38]

$$\frac{\partial^2 T}{\partial x^2}+\frac{\partial^2 T}{\partial y^2}+\frac{\partial^2 T}{\partial z^2}-\frac{1}{k}\frac{\partial T}{\partial t}=-\frac{q'''}{K} \tag{1}$$

where T is the temperature rise. K and k are respectively the thermal conductivity (W K^{-1} m^{-1}) and diffusivity (m^2 s^{-1}). Their relationship is $k=\frac{K}{\rho C}$. ρ is the density of the material (kg m^{-3}), and C is the specific heat of the material (J kg^{-1} K^{-1}). q''' is the heat produced per unit volume per unit time, in unit of W m^{-3}.

The instantaneous temperature rise from a point source [37] is

$$T(r,t)=\frac{Q}{8\rho C(\pi kt)^{3/2}}\exp\left(-\frac{r^2}{4kt}\right) \tag{2}$$

where Q is the total energy of the heat source (J), r is the radius in a polar coordinate (pole is the point source centre).

The instantaneous temperature rise from a line source [37] is

$$T(r,t)=\frac{Q'}{4\rho C\pi kt}\exp\left(-\frac{r^2}{4kt}\right) \tag{3}$$

where Q' is the energy per unit length in the line heat source (J m^{-1}).

A continuous heat source has the same effect as a sequence of a very large number of small instantaneous sources of equal size. Thus, for a point source with continuous heating and when Q is constant, the integrated temperature result in the time domain is [37]

$$\begin{aligned}T(r,t)&=\frac{Q}{8\rho C(\pi k)^{3/2}}\int_0^t\frac{\exp(-r^2/4kt')}{t'^{3/2}}\,\mathrm{d}t'\\&=\frac{q}{4\pi Kr}\operatorname{erfc}\left(\frac{r}{2(kt)^{1/2}}\right)\end{aligned} \tag{4}$$

where q is the source power (W).

For a line source with continuous heating, the integrated temperature result in the time domain is [37]

$$\begin{aligned}T(r,t)&=\frac{Q'}{4\rho C\pi k}\int_0^t\frac{\exp(-r^2/4kt')}{t'}\,\mathrm{d}t'\\&=\frac{q'}{4\pi K}\int_{r^2/4kt}^{\infty}\frac{\exp(-u)}{u}\,\mathrm{d}u\end{aligned} \tag{5}$$

where q' is the source power per unit length (W m^{-1}).

However, the 'cooling' effect after the laser spot or a laser line is switched off is not considered in equations (4) and (5). After convoluting the laser pulse (a square 'top-hat' shape in the time domain, Gaussian shape in the spatial domain) with the instantaneous temperature rise, for a Gaussian shape round spot source with continuous heating, the integrated temperature result in the time domain is [37, 39]

$$\begin{aligned}T(r,z,t)&=\frac{I_{\max}a^2k^{1/2}}{K\pi^{1/2}}\\&\times\int_0^t\frac{p(t-t')\exp(-z^2/4kt'-r^2/(4kt'+a^2))}{t'^{1/2}(4kt'+a^2)}\,\mathrm{d}t'\end{aligned} \tag{6}$$

where (r, z) are cylindrical coordinates with the origin on the surface at the centre of the irradiated spot. I_{max} is the maximum power density of the laser pulse, $p(t)$ is the normalized temporal profile of the laser pulse at the time t, and a is the laser beam radius.

For a Gaussian shape elliptical spot source with continuous heating, which is close to a line source when the long axial radius value b is much bigger than short axial radius a, the integrated temperature result in the time domain is [19, 28, 37, 39]

$$T(x, y, z, t) = \frac{I_{max} a b k^{1/2}}{K \pi^{1/2}} \times \int_0^t \frac{p(t-t')\exp(-z^2/4kt' - x^2/(4kt'+a^2) - y^2/(4kt'+b^2))}{t'^{1/2}(\sqrt{4kt'+a^2})(\sqrt{4kt'+b^2})} \, dt' \tag{7}$$

where (x, y, z) are Cartesian coordinates with the origin on the surface at the centre of the irradiated spot. I_{max} is the maximum power density of the laser pulse, $p(t)$ is the normalized temporal profile of the laser pulse at the time t. a and b are the laser beam radii.

2.2. 3D finite difference modelling

For 3D finite difference modelling, the heat boundary condition of the surface with laser-spot irradiation in Cartesian coordinates is

$$-K \frac{\partial T(x, y, z = 0, t)}{\partial z} = \frac{P}{\pi a^2} \exp[-(x^2 + y^2)/a^2]. \tag{8}$$

For the other five boundaries, we assume they are insulated. For example, at the boundary when $x = 0$, we have

$$\frac{\partial T(x = 0, y, z, t)}{\partial x} = 0. \tag{9}$$

The heat boundary condition of the surface with laser-line irradiation in Cartesian coordinates is

$$-K \frac{\partial T(x, y, z = 0, t)}{\partial z} = \frac{P}{\sqrt{\pi} a} \exp(-y^2/a^2). \tag{10}$$

The effects of cracks may be simulated by 'Ghost Points' in a numerical modelling grid that are generated by balancing thermal fluxes flowing into a crack and through a crack, with those flowing out of the crack according to Fourier's Law. They guarantee correct thermal gradients in the bulk material either side of the crack.

The concept of the 'ghost point' (or a fictitious point) in a 1D finite difference heat transfer model is shown in figure 1. In this case, the crack is embedded between the current grid point 'i' and its left grid point '$i - 1$'. The width of the crack 'δ' may be far smaller than the grid spacing 'd'. The distance of the crack to the left grid point is 'σ'. Usually, the crack is full of air and its conductivity 'K_a' is much lower than the conductivity of the metal block 'K_s'. Thus the thermal gradient across the crack will be larger than in the other parts of the metal block.

Equation (11) shows the heat flux balance in the x-direction when it flows from the grid point '$i - 1$' into the crack, through the crack and then flows out of the crack to the grid point 'i':

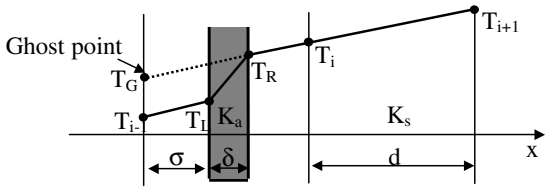

Figure 1. 1D 'ghost point' finite difference heat diffusion model. Heat flux is balanced when it flows into, through and out of the crack.

$$K_s \frac{T_L - T_{i-1}}{\sigma} = K_a \frac{T_R - T_L}{\delta} = K_s \frac{T_i - T_R}{d - \sigma - \delta} = g \tag{11}$$

where T_{i-1}, T_L, T_R, T_i and T_{i+1} are respectively the temperature rise at the grid point '$i - 1$', the left boundary of the crack, the right boundary of the crack and the grid points of 'i' and '$i + 1$'. g is the heat flux.

Equation (12) shows the calculation of the temperature rise at the 'ghost point'. By defining a 'ghost point' to equal the temperature increase effect because of the crack, the 'isotropic' heat transfer model can still be applied; however, the temperature rise at the grid point '$i - 1$' should be replaced by the value of the 'ghost point' T_G:

$$K_s \frac{T_i - T_G}{d} = g. \tag{12}$$

After substituting equation (11) into equation (12), we can represent T_G by T_i and T_{i-1}:

$$T_G = \frac{\xi}{\xi + d} T_i + \frac{d}{\xi + d} T_{i-1} \tag{13}$$

where ξ is related to K_s, K_a and δ:

$$\xi = \left(\frac{K_s}{K_a} - 1\right)\delta. \tag{14}$$

Equation (15) shows the 3D heat diffusion equation with no internal heat generation:

$$k\nabla^2 T = \frac{\partial T}{\partial t}. \tag{15}$$

Substituting equation (13) into equation (15), and representing equation (15) using finite difference elements, we can have

$$T^{n+1}_{i,j,m} = \frac{k \cdot \Delta t}{d^2} \cdot \left(T^n_{i+1,j,m} - a_c T^n_{i,j,m} + b_g T^n_{i-1,j,m} + N\right) + T^n_{i,j,m} \tag{16}$$

$$N = T^n_{i,j+1,m} + T^n_{i,j-1,m} + T^n_{i,j,m+1} + T^n_{i,j,m-1} \tag{17}$$

where Δt is the time step, $T^n_{i,j,m}$ is the temperature rise of the grid point 'i, j, m' at time n and $T^{n+1}_{i,j,m}$ is the temperature rise at the next time step. The values of a_c and b_g are

$$a_c = \frac{5\xi + 6d}{\xi + d} \tag{18}$$

$$b_g = \frac{d}{\xi + d}. \tag{19}$$

If the crack is embedded between the current grid point 'i, j, m' and the point '$i + 1, j, m$', then the grid point

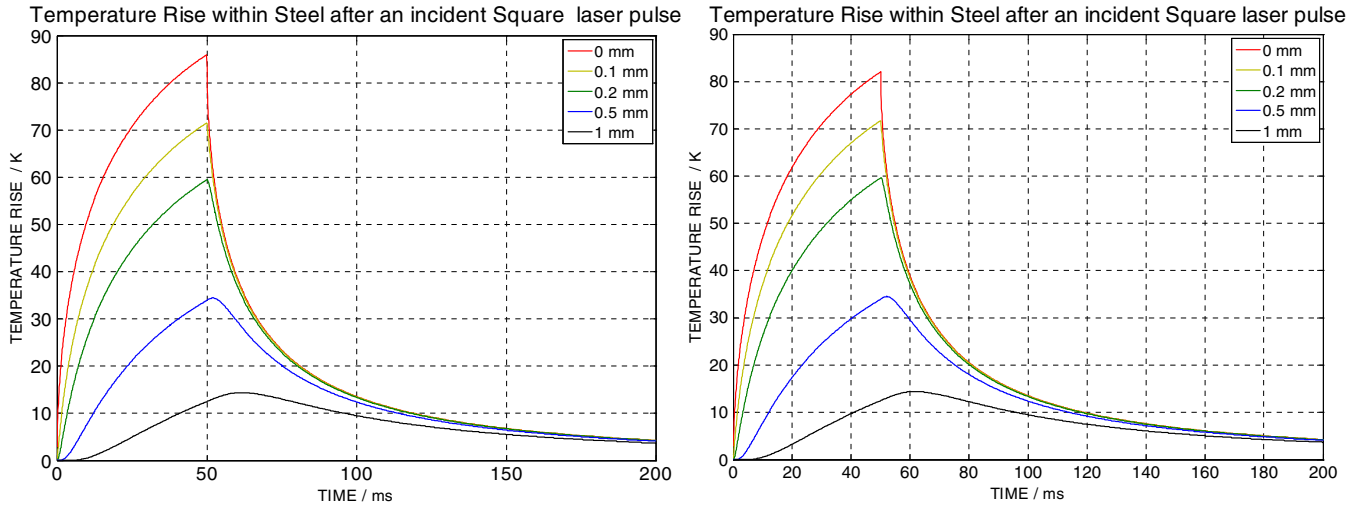

Figure 2. (*a*) 3D analytical modelling results. (*b*) 3D finite difference modelling results.

Table 1. Parameters used in the simulations.

Material	Thermal conductivity K (W m^{-1} K^{-1})	Specific heat C (J kg^{-1} K^{-1})	Mass density ρ (kg m^{-3})	Thermal diffusivity $k = K/\rho C$ (m^2 s^{-1})
Air	0.025	1000	1.205	2.0747×10^{-5}
Mild steel	40	500	7850	1.0191×10^{-5}
Stainless steel	13.5	485	7900	3.5234×10^{-6}

'$i+1$, j, m' becomes the 'ghost point' and the temperature rise at this point should multiply the coefficient b_g like the ghost point '$i-1$, j, m' in equation (16).

Furthermore, the temperature gradient across the crack can also be derived from equation (11) as follows:

$$\frac{T_R - T_L}{\delta} = \frac{T_i - T_{i-1}}{K_a/K_s(d-\delta)+\delta}. \tag{20}$$

By using the 'ghost points' to balance the heat flux, the heat transfer model avoids the need of the very fine mesh spacing that is necessary to deal with real cracks that often have openings of only a few micrometres [12, 13, 40]. In the following simulations, the boundary conditions for all metal samples are assumed to be insulation. The explicit finite difference method was employed with a 0.1 mm grid spacing and 0.1 ms time steps. The simulation programmes were formulated in MATLAB and run on a conventional PC. Table 1 shows the property parameters used in the simulations for the air gap and two kinds of steel.

2.3. 3D analytical and numerical results comparisons

In this section, 3D numerical modelling results will be compared with the analytical results when setting the crack width/opening to zero. We note that the values of ghost parameters of 'a_c' and 'b_g' will become '6' and '1' in equations (18) and (19) if we let $\delta = 0$, which turns the 'ghost point' model back to traditional 3D isotropic heat transfer model. In this way, the 3D ghost point method can be partially validated.

2.3.1. Temperature rise caused by a laser-spot source. Figure 2 shows the comparison of the 3D analytical modelling result and the 3D finite difference modelling results when the heating source is a laser spot. The laser pulse was a top hat (50 ms) in the time domain and a Gaussian spot shape in the spatial domain. The radius of the spot was taken to be 1 mm (1/e fall and $a = 1$ mm). The laser output power was 20 W, thus, $I_{\max} \approx 20/(\pi a^2) \approx 6.37 \times 10^6$ W m^{-2}. Note that the reflectivity of the sample surface was not considered in either model. That is, 20 W of power was assumed to be absorbed by metal samples. Lines with different colours in the figures correspond to temperatures rises of the laser-spot centre at different depths in the metal block. There is good agreement between the analytical and the modelling results. The only significant disagreement being a 3% difference in peak temperature at the surface, the 0 mm plots.

2.3.2. Temperature rise caused by a laser-line source. Figure 3 shows the comparison of the 3D analytical modelling results and the 3D finite difference modelling results when the heating source is a laser line. The laser pulse was a top hat (50 ms) in the time domain and a Gaussian elliptical shape in the spatial domain. The radius of the short axis was taken to be 1 mm (1/e fall and $a = 1$ mm), and the long axis radius was taken to be 10 mm (1/e fall and $b = 10$ mm). The laser output power was 20 W, thus, $I_{\max} \approx 20/(\pi ab) \approx 6.37 \times 10^5$ W m^{-2}. Again note that the reflectivity of the sample surface was not considered in either model. There is good general agreement between analytical and modelling results with peak temperature rises differing by only ~4%.

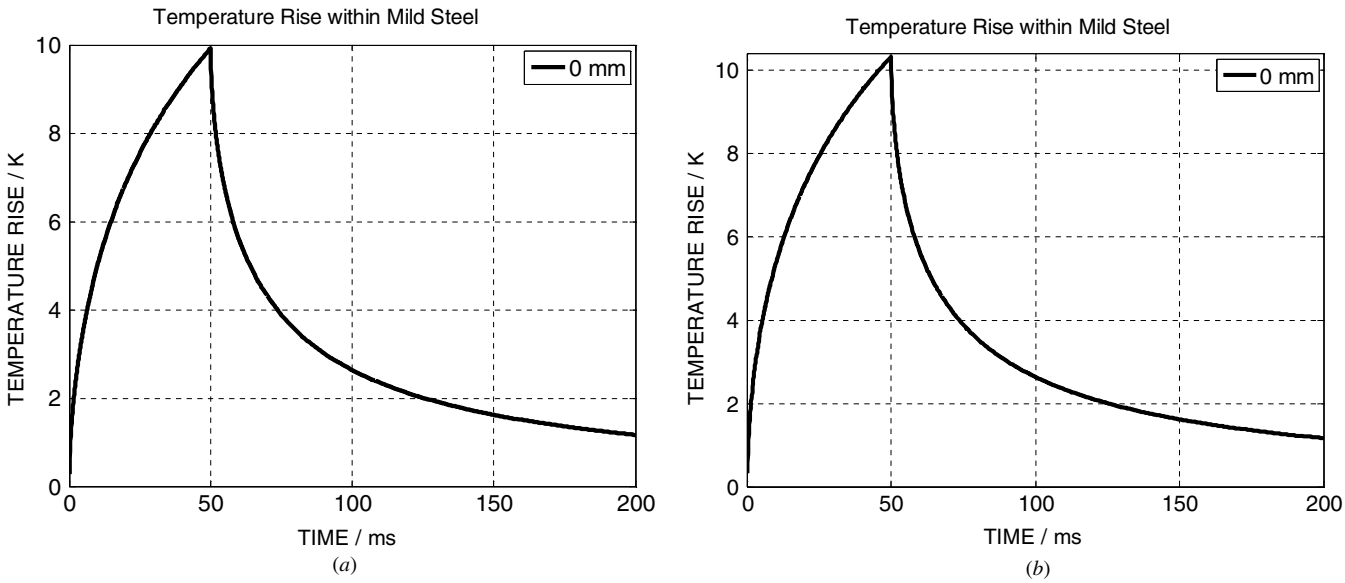

Figure 3. (*a*) 3D analytical modelling results. (*b*) 3D finite difference modelling results.

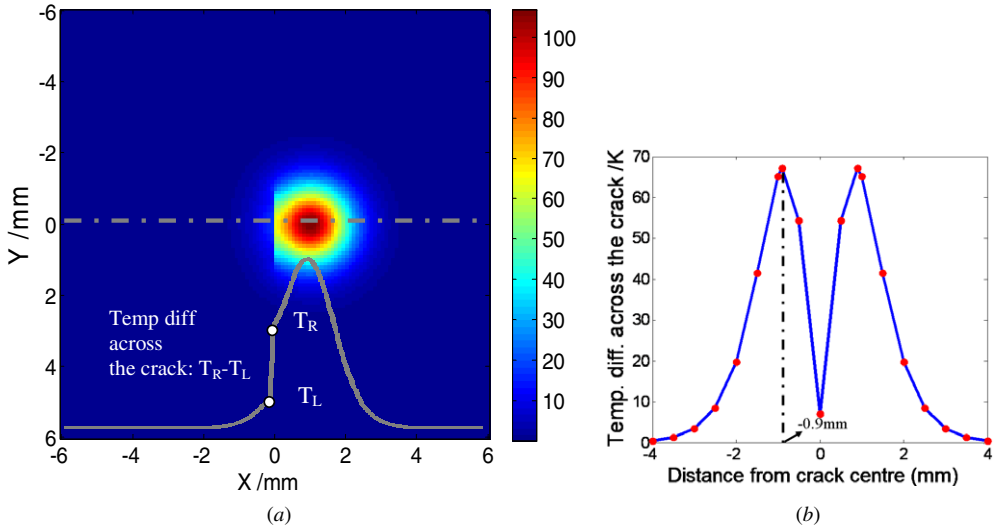

Figure 4. (*a*) Simulation of a laser-spot image after 50 ms heating. (*b*) Temperature difference across the crack as a function of the laser-spot distance to the crack.

2.4. Modelling results concerning the operating parameters and the geometries of a crack

Modelling has been used to gain an understanding of the optimum operating parameters for the LST and LLT techniques and to assess the theoretical limits of their sensitivities for the detection of cracks. Two kinds of cracks with different shapes (slot and half penny) have been used in the simulations and they were embedded vertically from the surface to a certain depth in a metal block (12 mm × 12 mm × 5 mm). The modelling grid spacing was 0.1 mm. In the modelling, the laser spot and the laser line are simulated scanning parallel to the *x*-axis and passing the centre of crack; the long axis of the laser line was parallel to the *y*-direction.

Before modelling, a metric will be first set to describe the crack heat blocking effect. Figure 4(*a*) shows the surface temperature obtained using the 3D ghost point finite difference model. The laser-spot duration was 50 ms and the output power was 21 W. The laser radius was 0.9 mm (1/e fall) and the crack was a slot crack embedded in a mild steel block, with opening 10 μm, length 2 mm and depth 2 mm. The solid grey line is the temperature profile across the crack and the laser-spot centre. The crack blockage effect can be quantified by the temperature difference or gradient across the crack. The temperature difference across the crack is adopted here as a metric of the crack heat-blocking effect. The effect of changing the distance of the laser-spot centre to the crack is shown in figure 4(*b*). It shows that the temperature difference metric reaches its largest value when the laser-spot centre is at a position of one radius of the laser beam from the crack. This position will be referred to as the 'optimum' position in this paper. Similarly, the simulated surface temperature produced

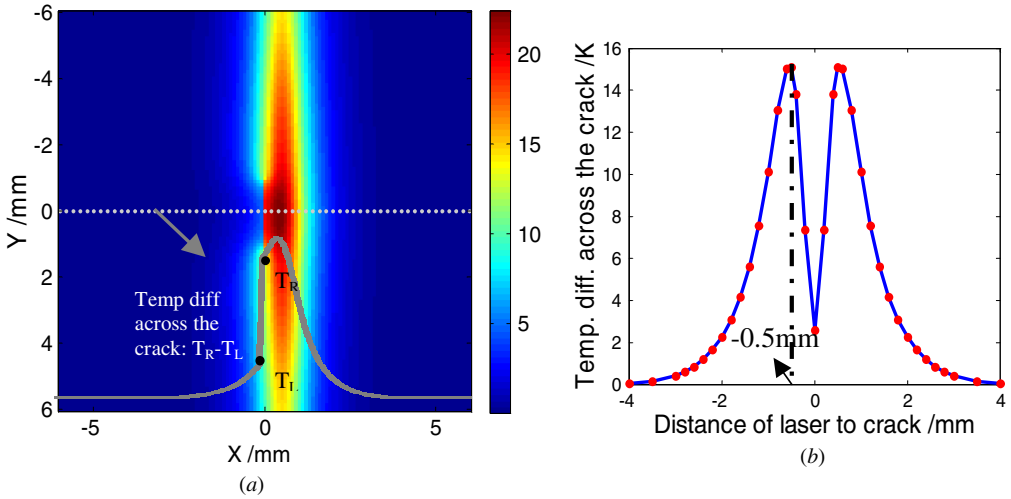

Figure 5. (*a*) Simulation of laser-line image after 100 ms heating. (*b*) Temperature difference across the crack as a function of the laser-line distance to the crack.

by a laser-line heating source parallel to the crack is shown in figure 5(*a*). The laser line was simulated by Gaussian elliptical shape in the spatial domain. The long axis radius was 10 mm (1/e fall) and the short axis radius was 0.5 mm (1/e fall). The laser pulse duration was 100 ms and the total laser output power and the crack geometries were kept the same. Figure 5(*b*) shows the variation of the temperature difference across the crack with the distance of the line source to the crack centre. Again, the 'optimum' imaging distance between the laser 'line' centre and the crack was one radius of the short axis.

Other operating parameters that will affect the temperature difference across the crack are laser power and pulse duration. For laser pulses with the same output energy it is found that the shorter the laser pulse, the higher the temperature difference across the crack that can be obtained. This is a result of the rapid thermal diffusion rate in metals that causes transient thermal perturbations to dissipate over a shorter time than the duration of the longer pulses. Balanced against this effect is a general increase in the crack thermal metric with laser pulse energy.

In addition, the crack geometry will affect the laser-spot and laser-line crack imaging. Figure 6 shows the variation of the temperature difference metric with: (*a*) crack opening, (*b*) crack length and (*c*) crack depth. These results are for the laser-line source that is shown in figure 5, at the optimum position and at the extinction of a 100 ms pulse. The results provide an indication of the limits of laser-line imaging for detecting cracks with certain geometries. They show a reduction in the temperature difference across the crack to occur when crack length is below ∼2 mm, crack depth is below ∼1 mm and crack opening is below ∼5 μm. These figures indicate that the technique, theoretically, has sensitivity adequate for many real inspection requirements. Very similar results are obtained for laser-spot heating [36].

3. Crack extraction based on modelling and experimental results

Results for the laser-line source are presented here. Those for the laser spot have been presented elsewhere [36].

3.1. Crack imaging by a static laser line

The 3D ghost point finite difference model has helped to establish the limits of the effectiveness of LST and LLT in the detection of cracks with opening in the micrometre range. In addition, this 3D model has helped the development of a new crack imaging method. The purpose of this method is to obtain an image of the crack from the effects it has had on the thermal images of a nearby laser-heated spot. A common image processing technique is to compute the first spatial derivative which reflects the amplitude change rate in an image and thus extracts edges in images. The perturbation of a laser-spot image caused by a crack can be regarded in the same way as an edge feature. However, the background heat flow caused by the focused laser spot is still strong and causes large thermal gradients that are mixed together with the crack effects when the spot is close to the crack. The 'second spatial derivative' has also been considered since it has been found to enhance the crack effects whilst reducing those of the laser spot.

Figure 7(*a*) shows the normalized first (blue dashed line) and second (red solid line) derivatives of the temperature profile line plotted in figure 5(*a*). The red line in figure 7(*a*) shows the improved crack discrimination obtained from second derivative processing. Figures 7(*b*) and (*c*) show normalized 2D images obtained using the first and second-derivative image processing of the data shown in figure 5(*a*) (derivatives taken in the *x*-direction perpendicular to the crack). It is clear that the second derivative processing provides a better means of isolating the image of the crack. The contrast of the crack to the background heat flow (ratio of the maximum amplitude at crack positions to the maximum amplitude of the

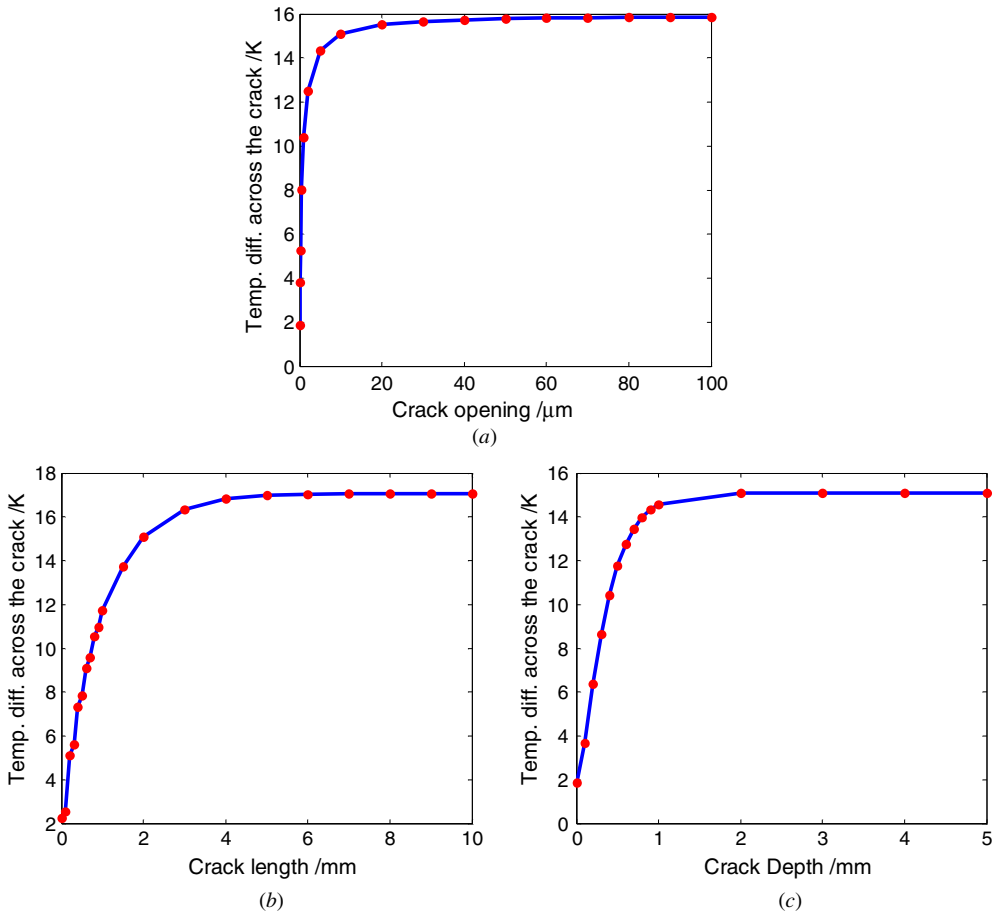

Figure 6. Temperature difference across a crack for a laser-line source when (*a*) crack opening changes, (*b*) crack length changes and (*c*) crack depth changes.

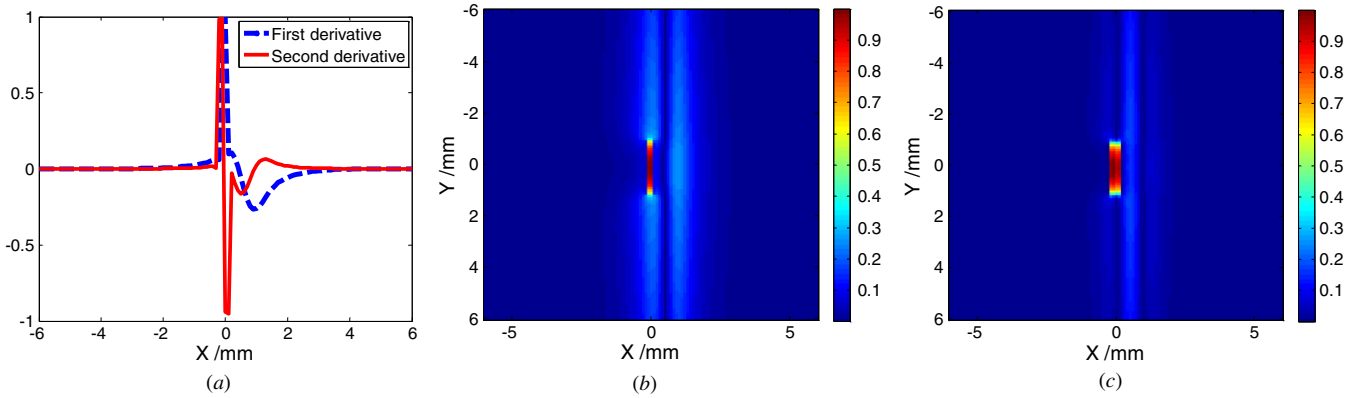

Figure 7. (*a*) Normalized first (blue line) and second (red line) spatial derivatives of the temperature profile line in figure 5(*a*). (*b*) First-derivative image, in the *x*-direction, of the image in figure 5(*a*). (*b*) Second-derivative image, in the *x*-direction, of the image in figure 5(*a*).

background heat flow) in figure 7(*c*) is 1.65 times higher than that shown in figure 7(*b*).

In practice, the image acquisition time and noise need to be considered. The simulation shown in figure 5(*a*) corresponds to images that might be collected by a thermal imaging camera just at the time of the extinction of a laser heating pulse. In practice, more thermal images at different times can be used. This provides the opportunity to form a summed thermal image that will further emphasize the crack structure over the background heat flow. However, the second-derivative method is known to be sensitive to the noise [41], so only thermal images with a high signal-to-noise ratio should be considered. The effects of image addition and noise were investigated by adding ±0.1 K (one standard deviation) of random noise to the above model and summing first-derivative thermal images, and then second, from 0.1 s, the time of extinction of the laser

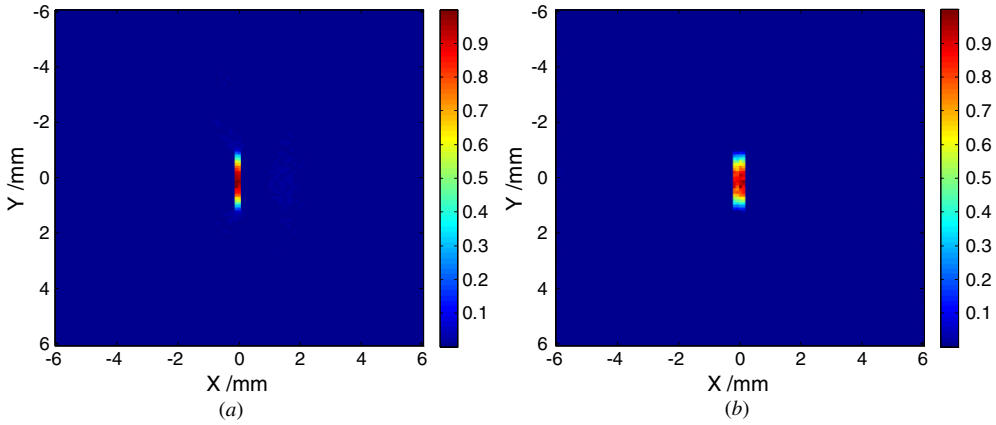

Figure 8. (*a*) Summed first-derivative image in the *x*-direction from 0.1 to 0.3 s. (*b*) Summed second-derivative images in the *x*-direction from 0.1 to 0.3 s. The noise level was ±0.1 K.

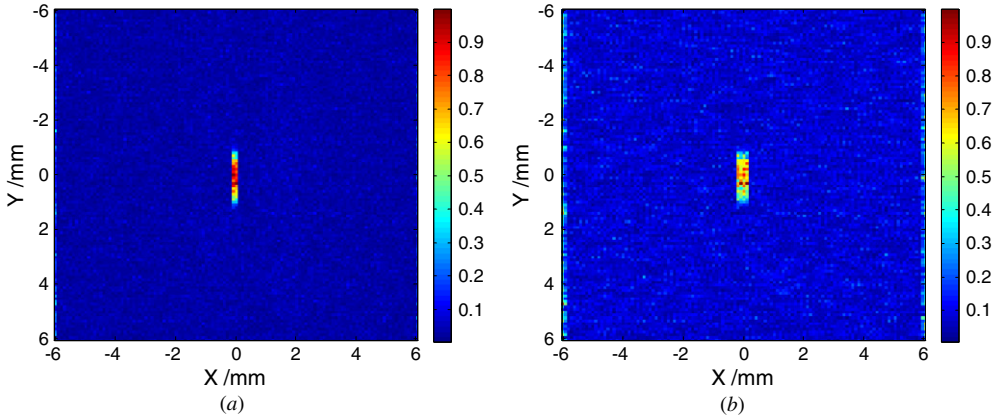

Figure 9. (*a*) Summed first-derivative image in the *x*-direction from 0.1 to 0.3 s. (*b*) Summed second-derivative image in the *x*-direction from 0.1 to 0.3 s. The noise level was ±0.5 K.

heating pulse, to 0.3 s, when the remaining heating became comparable to the noise level. Images were computed at intervals of 1/60 s matching the 60 Hz frame rate of the IR camera used in the experimental work below. The normalized first and second-derivative images are shown in figures 8(*a*) and (*b*), respectively. After integrating thermal images, the contrast of the crack to the background heat flow in figure 8(*b*) is 1.98 times higher than figure 8(*a*).

However, when the noise was increased to ±0.5 K, the second-derivative method becomes affected more by the noise than the first-derivative method, which is shown in figure 9. After integrating thermal images, the contrast of the crack to the background heat flow in figure 9(*a*) (first derivative) is 3.61 times higher than figure 9(*b*) (second derivative).

3.2. Theoretical crack imaging by scanning laser line

The above simulation results demonstrate the crack-imaging ability when the laser-line source is parallel to the crack. However, simulations also show that the crack cannot be detected if it is perpendicular to the line heat source. In practice, the crack orientation is unknown. The effect of a crack orientated at 45° to the laser line is shown in figures 10 and 11. The crack was a half-penny-shaped crack of length 5 mm, depth 2 mm and width 1 μm. The laser long axis radius was 10 mm (1/e fall) and the short axis radius was 0.5 mm (1/e fall). The laser pulse duration was 100 ms. It may be seen that only part of the crack can be detected at the two static positions of the laser line. In practice, the location of a crack would be unknown and line scanning in two orthogonal directions would be used. The combination of the results obtained from such scans would improve the sizing of cracks, as shown in the experimental work, below.

Figure 12(*a*) shows a simulation of the laser-line thermal images that would be used to scan the whole block with an orientation of 45° to the crack, using a scan step length of twice the laser beam radius (1.8 mm). The first and second-derivative (*x*-direction) images, figures 12(*b*) and (*c*), result in a broken image of the crack. Figure 13 shows a similar scan using a step size of one laser beam radius, resulting in the complete first and second-derivative images of the whole of the crack, figures 13(*b*) and (*c*).

Based on these simulation studies, an image processing procedure has been formulated. The processing steps performed on the thermal images from the IR camera are as follows.

(1) Subtract the background IR image to produce a dark-field image showing only the transient heat diffusion (this can

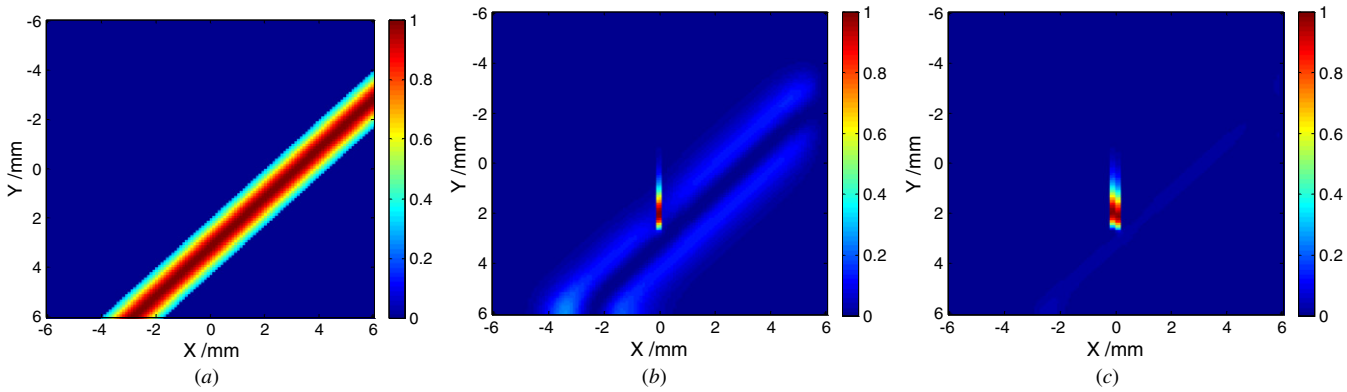

Figure 10. Laser-line source crossing the tip of the crack. (*a*) Simulation of the thermal image of the laser line. (*b*) First differential image. (*c*) Second differential image.

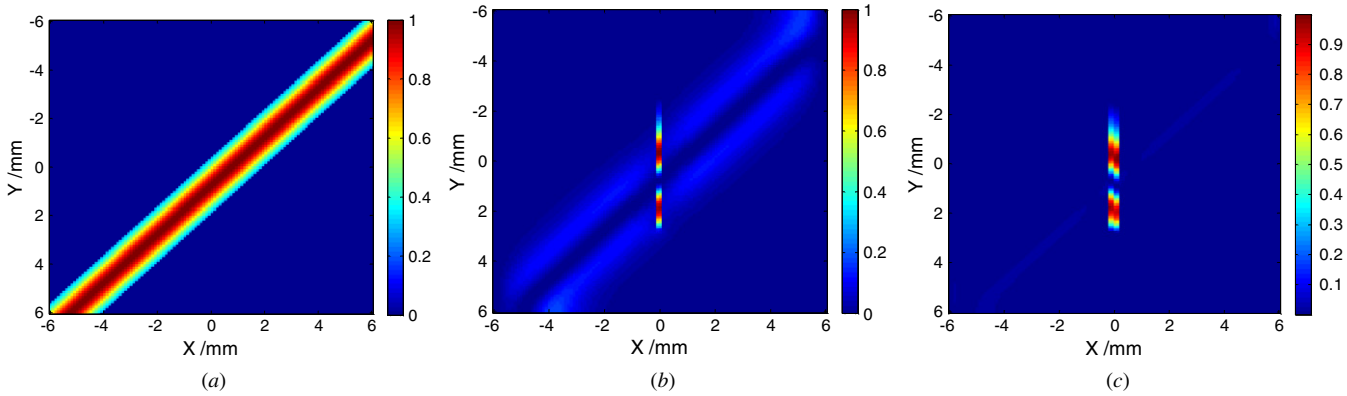

Figure 11. Laser-line source crossing the centre part of the crack. (*a*) Simulation of thermal image of the laser line. (*b*) First differential image. (*c*) Second differential image.

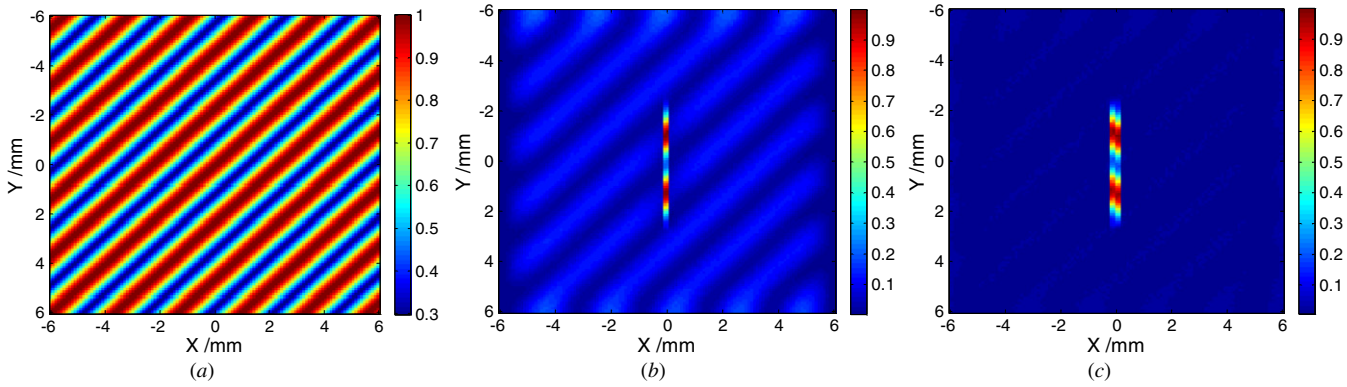

Figure 12. Laser-line source scans across the block using a 2× laser beam radius step length. (*a*) Simulations of thermal images of the laser line at each scan position. (*b*) Cumulative first differential image. (*c*) Cumulative second differential image.

be easily done by subtracting a thermal image obtained before the laser was switched on).

(2) Compute the first and second derivative of each dark-field image at each scanning step in both the *x*- and *y*-directions.

(3) Integrate all derivative images in the *x*- and *y*-directions collected from 0.1 to 0.3 s at each scanning position.

(4) Form a composite image of all the integrated images obtained at the different scanning positions. A final summed image may be obtained by adding the squares of the two derivative images in the *x*- and *y*-directions.

4. Experimental crack imaging by scanning LLT

Figure 14(*a*) shows the experimental setup for scanning laser-line thermography. A beam expander (seven times) and a cylindrical lens were used to convert a laser spot with a radius of around 0.9 mm to a laser-line source. Figure 14(*b*) shows the thermal image of the heating produced by the laser-line source. Its length was around 15 mm (1/e fall) and its width was about 0.5 mm (1/e fall).

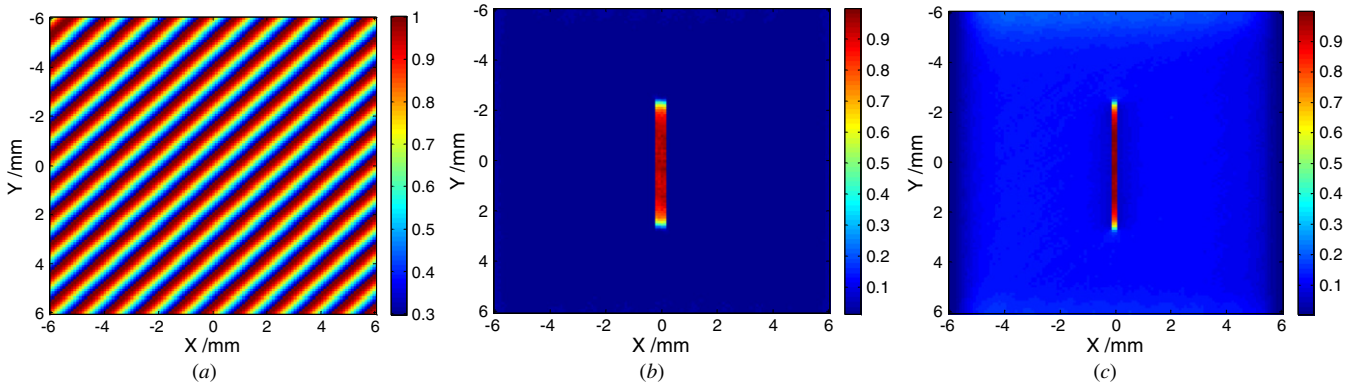

Figure 13. Laser-line source scans across the block using a 1× laser beam radius step length. (*a*) Simulations of thermal images of the laser line at each scan position. (*b*) Cumulative first differential image. (*c*) Cumulative second differential image.

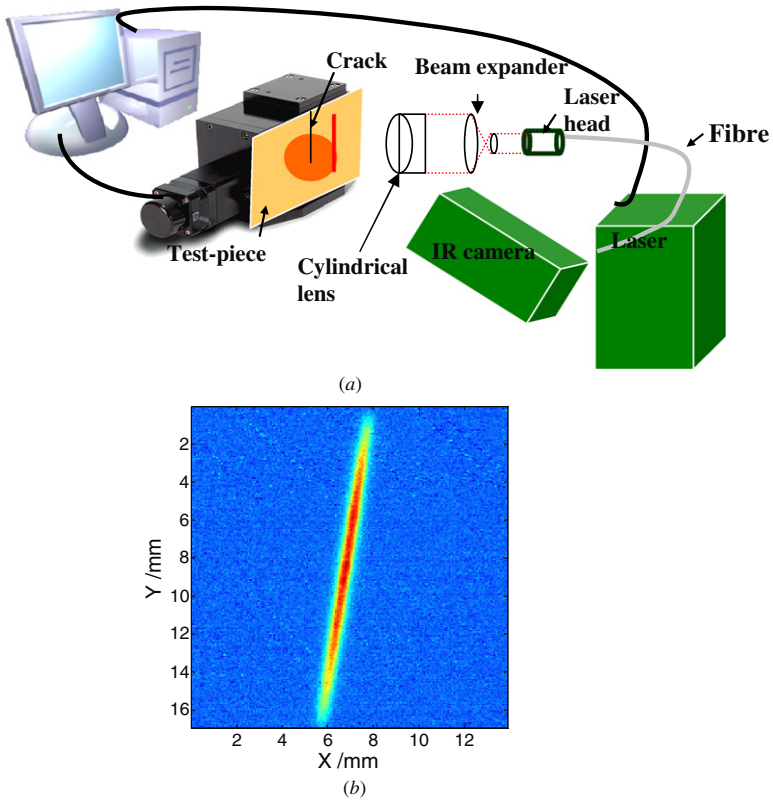

Figure 14. (*a*) Experimental setup for the laser-line scanning. (*b*) Thermal image of the obtained laser line (around 15 mm long, 1/e fall).

Figure 15(*a*) shows a set of nine experimental thermal images obtained by a 60 Hz frame rate IR camera following the extinction of a 100 ms laser heating pulse. The test piece was a stainless steel plate with a crack at the surface centre (10 mm long, 2 mm deep, and 50 μm wide). The laser line was set at the optimum position to the right of the crack. Corresponding simulated thermal images are shown in figure 15(*b*). A thermal noise level of ± 1 K was added to the thermal images in the simulations. The simulations can be seen reproduce all the principle features of the experimental results.

The crack images, figures 16(*a*) and (*b*), were obtained using the image processing method defined in section 3. The crack was in a titanium test piece; it was 11 mm long with a depth at the crack centre of about 3 mm. The crack was opened, using a three-point bending rig, to produce an average opening of the crack of 20 μm. The reflectivity of the surface was smaller than 40%. The crack was orientated at an angle of approximately 45° to test the ability of the technique to image cracks at an angle to the scanning direction. The laser line was scanned in the *x*-direction with a step length of 0.2 mm. The total scan length in the *x*-direction was 10 mm. Figure 16(*a*) shows the first-derivative image and figure 16(*b*) shows the second-derivative image. The crack shape shown in the thermal images compared well with the microscope photographs of the crack. Information about the distribution of the crack opening can also be seen in the image; it shows stronger signals in the middle part of the crack, where the crack is most open.

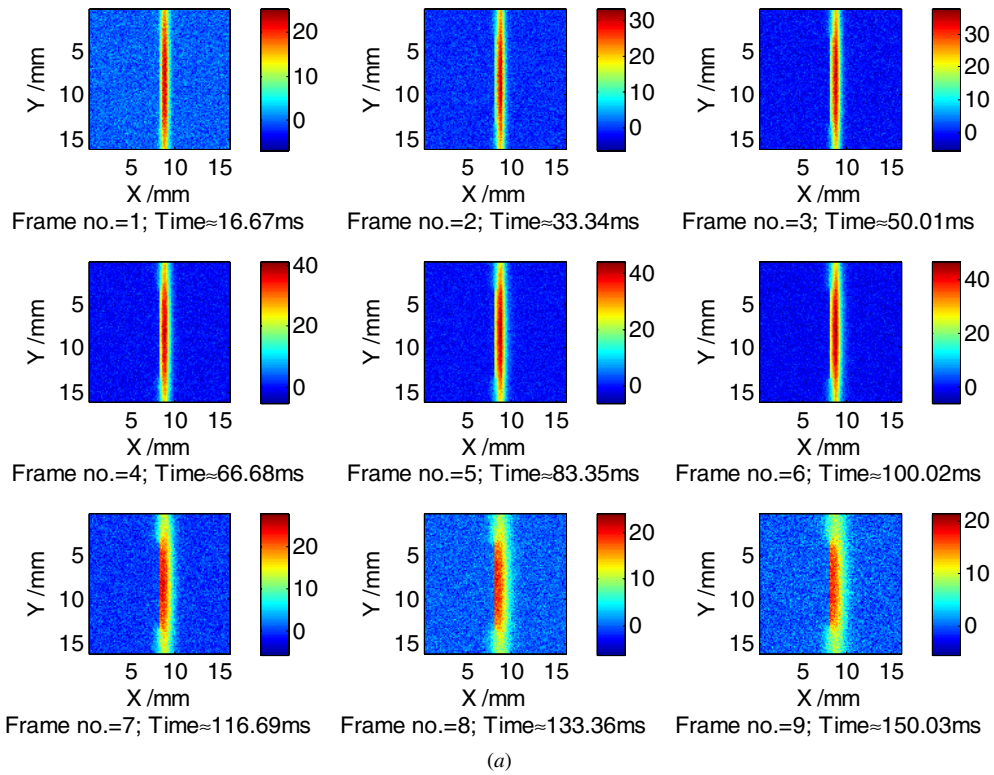

(*a*)

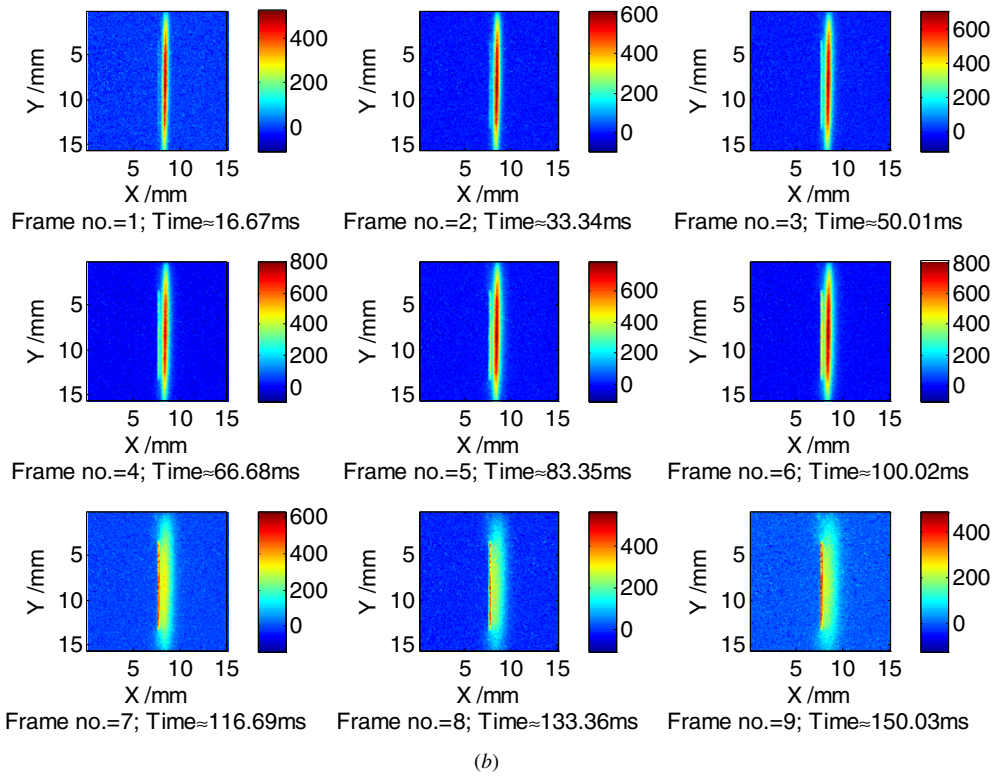

(*b*)

Figure 15. (*a*) Experimental laser-line thermal images of a crack of 10 mm length, 2 mm depth and 50 μm width in a stainless steel plate. (*b*) Corresponding simulated thermal images.

The advantage of the laser-line scanning technique over the laser-spot scanning technique is a significant reduction in scanning time. For the same scanning area (10 × 10 mm), using the same 0.2 mm *x*-direction scan steps and *y*-direction steps of 0.5 mm, 1000 scan steps are required by LST to scan the area, whilst only 50 scan steps are needed to generate an LLT image. Consequently, the scanning time for LST would be 20 times longer than LLT, for this case. In addition,

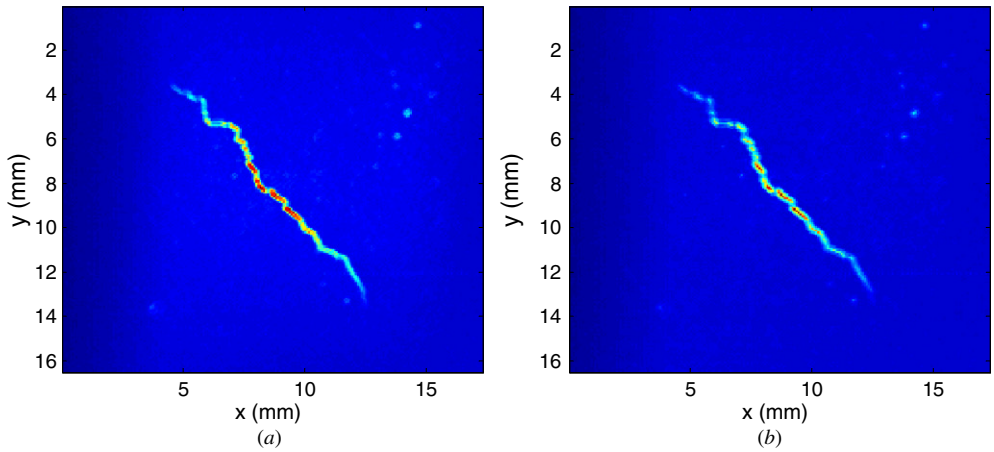

Figure 16. (*a*) Summed first-derivative thermal images of a crack using the laser-line source. (*b*) Summed second-derivative thermal image.

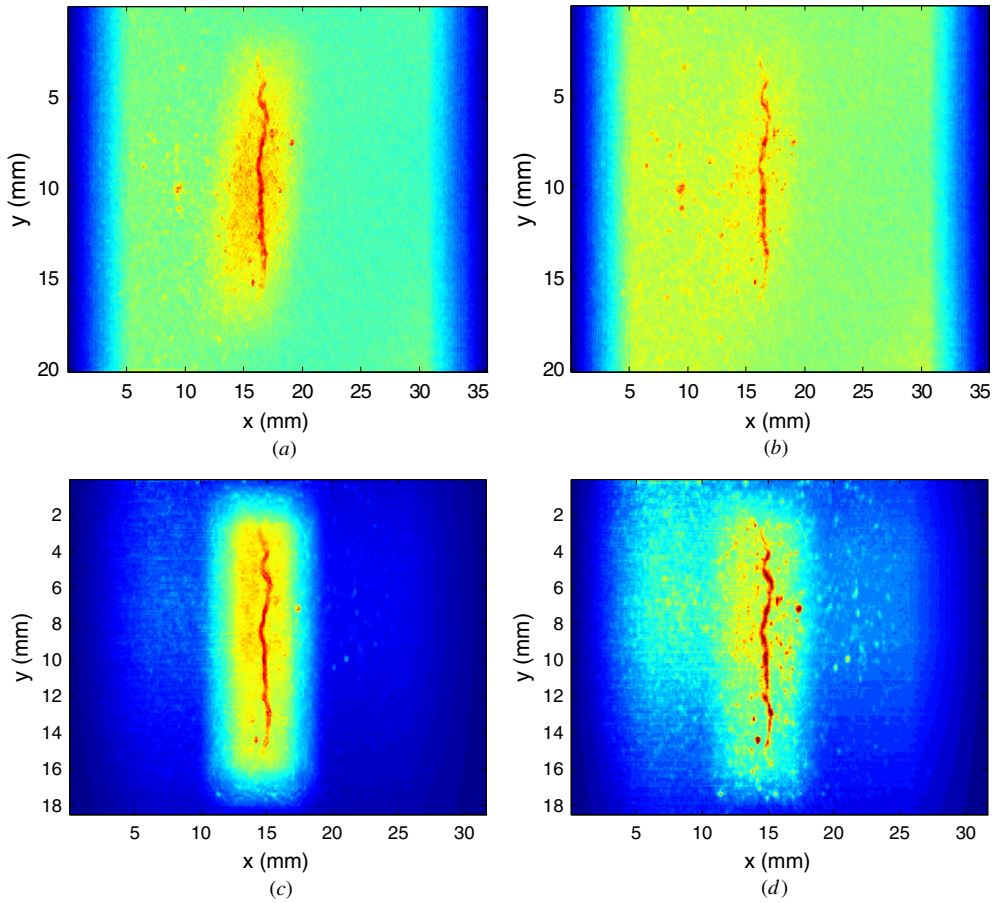

Figure 17. Titanium test piece with a crack of 11 mm long, 3 μm wide. (*a*) Summed first-derivative imaging result by the LLT method. (*b*) Summed second-derivative imaging result using the LLT method. (*c*) Summed first-derivative imaging result by the LST method. (*d*) Summed second-derivative imaging result by the LST method.

experimental results show that both LLT and LST obtained first- and second-derivative images with similar signal-to-noise ratios.

Derivative images of the same crack without applying the three-point bending force to the titanium test piece, which resulted in an average crack opening of $\sim$3 μm, are shown in figure 17. Figures 17(*a*) and (*b*) are the imaging results which were obtained using LLT. Figures 17(*c*) and (*d*) are imaging results obtained using LST. The crack shape and size are clear in all four images. This provides evidence of the sensitivities of the techniques to cracks with openings of a few micrometres. The LST image SNRs were slightly higher than those of the LLT images because of the higher laser output power density of the focused, unexpanded, laser spot.

The scan steps of both LLT and LST in the x-direction were 0.2 mm. The total scan lengths were around 6 mm in the x-direction for both LLT and LST. In the y-direction, the scan step was 0.5 mm for LST and the total scan length was around 15 mm. Thus the scan time of LST was 30 times longer than that of LLT.

5. Discussion and conclusions

The results presented in this paper indicate that both LST and LLT techniques have sensitivities to cracks that are competitive with many established NDE techniques. The techniques have the advantages of being non-contactive and requiring no surface preparation. However, it is known that for the techniques to be successful, surfaces should be clean and free of deep scratches or indentations that would perturb heat flow in a similar manner to a crack.

The paper also presents a derivative image processing method for extracting images of cracks after line or raster scanning. The results obtained show scanned pulse LLT and LST, incorporating derivative image processing, to be a new effective nondestructive evaluation technique for detecting and imaging surface breaking cracks with openings in the range of micrometres. Crack images obtained by the new techniques are at least comparable to those obtained by the long established dye penetrant inspection (DPI) method. However, this new technique has the advantages of eliminating the long preparation time of the DPI technique, of eliminating the use of undesirable liquids, of eliminating the exposure of the inspector to UV light, of being deployable remotely and of being suitable for automation. The practical sensitivities and reliabilities of the new techniques are under investigation.

The LLT method provides much higher scanning rate than the LST method. The fundamental limit to the scanning rate is the laser excitation time that was 100 ms for the LLT method. This time is a function of available laser power and line length as an adequate energy density has to be deposited to achieve images of acceptable signal-to-noise ratios. In the system employed in this work, the time taken to write IR camera data collected at each raster position to the main system control computer set the scanning rate. There would be considerable scope for reducing this time constraint if a fully integrated and optimized system was developed but this was outside the scope of this work which has demonstrated the operating principles of the LLT imaging method. Subsequent image processing time was negligible. However, it is recognized that this technique is still far slower than pulsed transient thermography using flash lamps and that its areas of application will probably be the inspection of localized defect-prone areas on comparatively small components. For both techniques the equipment cost is dominated by the cost of the IR camera, in the case of LLT being a factor of about three higher than the cost of the laser and scanning stage combined.

Acknowledgments

This research was funded as a targeted research project of the Engineering and Physical Science Research Council (EPSRC) UK Research Centre in NDE (RCNDE). The work also received support from Rolls Royce plc, RWE Npower and the National Nuclear Laboratory.

References

[1] Reynolds W N 1986 Thermographic methods applied to industrial materials *Can. J. Phys.* **64** 1150–4

[2] Milne J M and Reynolds W N 1984 The nondestructive evaluation of composites and other materials by thermal pulse video thermography *Proc. SPIE* **520** 119–22

[3] Lau S K, Almond D P and Milne J M 1991 A quantitative analysis of pulsed video thermography *NDT&E Int.* **24** 195–202

[4] Shepard S M, Lhota J R and Ahmed T 2007 Flash thermography contrast model based on IR camera noise characteristics *Nondestruct. Test. Eval.* **22** 113–26

[5] Rantala J, Hartikainen J and Jaarinen J 1990 Photothermal determination of vertical crack lengths in silicon nitride *Appl. Phys.* A **50** 465–71

[6] Brandis E and Rosencwaig A 1980 Thermal wave microscopy with electron beams *Appl. Phys. Lett.* **37** 98–100

[7] Rose D N, Turner H and Legg K O 1986 Ion acoustic microscopy *Can. J. Phys.* **64** 1284–6

[8] Wang Y Q, Kuo P K, Favro L D and Thomas R L 1990 Flying laser spot thermal wave IR imaging of horizontal and vertical cracks *Review of Progress in QNDE* vol 9A ed D O Thompson and D E Chimenti (New York: Plenum) pp 511–6

[9] Wang Y Q, Chen P, Kuo P K, Favro L D and Thomas R L 1992 Flying spot thermal wave IR imaging of horizontal and vertical cracks *Review of Progress in QNDE* vol 11A ed D O Thompson and D E Chimenti (New York: Plenum) pp 453–6

[10] Krapez J C, Gruss C, Huttner R, Lepoutre F and Legrandjacques L 2001 La caméra photothermique—partie I. Principe, modélisation, application à la détection de fissures *Instrum. Mes. Metrologie* **1** 9–39 (in French)

[11] Krapez J C, Lepoutre F, Huttner R, Gruss C, Legrandjacques L, Piriou M, Gros J, Gente D, Hermosilla-Lara S, Joubert P Y and Placko D 2001 La caméra photothermique—partie II. Applications industrielles, perspectives d'amélioration par un nouveau traitement d'image *Instrum. Mes. Metrologie* **1** 41–67 (in French)

[12] Rashed A, Almond D P, Rees D A S, Burrows S and Dixon S 2007 Crack detection by laser spot imaging thermography *Review of Progress in QNDE* vol 26 ed D O Thompson and D E Chimenti (New York: Plenum) pp 500–6

[13] Burrows S E, Rashed A, Almond D P and Dixon S 2007 Combined laser spot imaging thermography and ultrasonic measurements for crack detection *Nondestruct. Test. Eval.* **22** 217–27

[14] Kuo P K, Hartikainen J, Oppenheim I C, Favro L D, Feng Z J and Thomas R L 1988 Thermal wave characterization of coated surfaces using an IR video camera and a scanned heat source *Review of Progress in QNDE* vol 7A ed D O Thompson and D E Chimenti (New York: Plenum) pp 273–7

[15] Kuo P K, Oppenheim I C, Favro L D, Feng Z J, Thomas R L, Hartikainen J and Inglehart L J 1988 Time-resolved IR video imaging with synchronized scanned laser heating *Springer Series in Optical Sciences* vol 58 ed P Hess and J Pelzl (Berlin: Springer) pp 496–9

[16] Jaarinen J, Reyes C B, Oppenheim I C, Favro L D, Kuo P K and Thomas R L 1987 Thermal wave characterization of coated surfaces *Review of Progress in QNDE* vol 6B

ed D O Thompson and D E Chimenti (New York: Plenum) pp 1347–51
[17] Saniie J, Luukkala M, Lehto A and Rajala R 1982 Thermal wave imaging through radio frequency induction heating *Electron. Lett.* **18** 651–3
[18] Lehtiniemi R, Hartikainen J, Varis J and Luukkala M 1992 Induction heating as a selective heat source in fast thermal non-destructive evaluation *Photoacoustic and Photothermal Phenomena III* vol 69 ed D Bicanic (Berlin: Springer) pp 512–5
[19] Varis J 1998 Infrared line-scanning technique for thermal non-destructive testing of carbon fiber reinforced composites *Acta Polytechnica Scandinavica Appl. Phys. Series no. 215* (Espoo: Finnish Academy of Technology)
[20] Varis J, Lehtiniemi R, Hartikainen J and Rantala J 1995 Transportable infrared line scanner based equipment for thermal non-destructive testing *Res. Nondestruct. Eval.* **6** 85–97
[21] Varis J, Lehtiniemi R, Rantala J and Hartikainen J 1996 An infrared line scanning technique for detecting vertical cracks in carbon fibre tubes *NDT&E Int.* **29** 371–7
[22] Lehtiniemi R, Rantala J and Hartikainen J 1995 Photothermal line scanning system for the NDT of plasma sprayed coatings of nuclear plant components *Res. Nondestruct. Eval.* **6** 99–123
[23] Maldague X P V 2001 *Theory and Practice of Infrared Technology for Nondestructive Testing* (New York: Wiley-Interscience)
[24] Varis J, Rantala J and Hartikainen J 1995 A numerical study on the effects of line heating in layered anisotropic carbon fibre composites *Res. Nondestruct. Eval.* **6** 69–83
[25] Varis J and Lehtiniemi R 1997 Thermal non-destructive evaluation system for detecting vertical cracks in unidirectional carbon fibre composite *Rev. Sci. Instrum.* **68** 2818–21
[26] Inglehart L J, Grice K R, Favro L D, Kuo P K and Thomas R L 1983 Spatial resolution of thermal wave microscopes *Appl. Phys. Lett.* **43** 446–8
[27] Grice K R, Inglehart L J, Favro L D, Kuo P K and Thomas R L 1983 Thermal wave imaging of closed cracks in opaque solids *J. Appl. Phys.* **54** 6245–55
[28] Nissim Y I, Lietoila A, Gold R B and Gibbons J F 1980 Temperature distributions produced in semiconductors by scanning elliptical or circular cw laser beam *J. Appl. Phys.* **51** 274–9
[29] Busse G 1985 Imaging with opticvally generated thermal waves *IEEE Trans. Sonics Ultrason.* **32** 355–64
[30] Bodnar J L, Menu C, Egée M, Pigeon P and Le Blanc A 1993 Detection of wear cracks by photothermal radiometry *Wear* **162–164** (Part A) 590–2
[31] Boccara A C, Fournier D, Guitonny J, Liboux M Le and Mansanares A M 1992 Differential stimulated infrared radiometry: application to remote detection of cracks *Int. Conf. on Quantitative InfraRed Thermography (Chatenay-Malabry, Paris, France)* pp 382–7
[32] Kaufman I and Choudhury A K 1985 Radiometric crack detection in fast moving surfaces *Appl. Phys. Lett.* **46** 152–4
[33] Kaufman I, Chang P T, Hsu H S, Huang W Y and Shyong D Y 1987 Photothermal radiometric detection and imaging of surface cracks *J. Nondestruct. Eval.* **6** 87–100
[34] Bodnar J L and Egée M 1996 Wear crack characterisation by photothermal radiometry *Wear* **196** 54–9
[35] Ahn J W, Maingi R, Mastrovito D and Roquemore A L 2010 High speed infrared camera diagnostic for heat flux measurement in NSTX *Rev. Sci. Instrum.* **81** 023501
[36] Li T, Almond D P, Rees D A S, Weekes B and Pickering S G 2010 Pulsed laser spot imaging thermography, modeling and experimental data *Review of Progress in QNDE* vol 29A ed D O Thompson and D E Chimenti (New York: Melville) 435–42
[37] Carslaw H S and Jaeger J C 1959 *Conduction of Heat in Solids* (London: Oxford University Press)
[38] Almond D P and Patel P M 1996 *Photothermal Science and Techniques* (London: Chapman & Hall)
[39] Ready J F 1971 *Effects of High-Power Laser Radiation* (New York: Academic)
[40] Rantala J and Hartikainen J 1991 Numerical estimation of the spatial resolution of thermal NDT techniques based on flash heating *Res. Nondestruct. Eval.* **3** 125–39
[41] Gonzalez R C and Woods R E 2006 *Digital Image Processing* (Englewood Cliffs, NJ: Prentice Hall) pp 702–5